PAPER

Check for updates

Facile synthesis of Ni/NiO nanocomposites: the effect of Ni content in NiO upon the oxygen evolution reaction within alkaline media†

Srinivasa N.,[a] Jack P. Hughes,[bc] Prashanth S. Adarakatti, [ID][cd] Manjunatha C., [ID][e] Samuel J. Rowley-Neale, [ID][bc] Ashoka S. [ID]*[a] and Craig E. Banks [ID]*[bc]

We present the facile synthesis of Ni/NiO nanocomposites, *via* a solution combustion methodology, where the composition of metallic Ni within NiO is controlled by varying the annealing time, from 4 minutes up to 8 hours. The various Ni/NiO nanocomposites are studied *via* electrically wiring them upon screen-printed graphite macroelectrodes by physical deposition. Subsequently their electrochemical activity, towards the oxygen evolution reaction (OER), is assessed within (ultra-pure) alkaline media (1.0 M KOH). An optimal annealing time of 2 hours is found, which gives rise to an electrochemical oxidation potential (recorded at 10 mA cm^{-2}) of 231 mV (*vs.* Ag/AgCl 1.46 *vs.* RHE). These values show the Ni/NiO nanocomposites to be significantly more electrocatalytic than a bare/unmodified SPE (460 mV *vs.* Ag/AgCl). A remarkable percentage increase (134%) in achievable current density is realised by the former over that of the latter. Tafel analysis and turn over frequency is reported with a likely underlying mechanism for the Ni/NiO nanocomposites towards the OER proposed. In the former case, Tafel analysis is overviewed for general multi-step overall electrochemical reaction processes, which can be used to assist other researchers in determining mechanistic information, such as electron transfer and rate determining steps, when exploring the OER. The optimal Ni/NiO nanocomposite exhibits promising stability at the potential of +231 mV, retaining near 100% of its achievable current density after 28 hours. Due to the facile and rapid fabrication methodology of the Ni/NiO nanocomposites, such an approach is ideally suited towards the mass production of highly active and stable electrocatalysts for application within the anodic catalyst layers of commercial alkaline electrolysers.

1. Introduction

Renewable energy-driven electrolytic water splitting is the most promising approach to produce hydrogen to support a green energy infrastructure. Green hydrogen gas when produced *via* electrolytic water splitting, with the required energy being supplied from renewable sources, is considered a promising clean energy carrier due to its high energy density in comparison to fossil fuel counterparts, with the benefit of no direct carbon emissions.[1]

Electrolytic water splitting within alkaline conditions is potentially the cheapest method of hydrogen production, due to its low energy consumption, low cost and the long lifetime of the electrolyser cell components.[2] This is in comparison to electrolysis in acidic conditions or proton exchange membrane (PEM) electrolysis, where there is typically a requirement for costly cell components such as the catalyst layers and bipolar plates; this is exacerbated by the operating conditions within a PEM cell leading to component corrosion.[3,4] Electrolytic water splitting within an alkaline electrolyser, where ideally, water is turned into hydrogen and oxygen, requires two major reactions, namely the cathodic hydrogen evolution reaction (HER) and the anodic oxygen evolution reaction (OER). A theoretical thermodynamic cell voltage of +1.23 V (*vs.* RHE) is required for the overall reaction to occur, where any additional potential over this, is termed as the overpotential and represents the thermodynamic inefficiencies within the electrolyser cell.[5] Many studies have compared the alkaline OER activity of non-precious metal (NPM) based anodic electrocatalysts to benchmark precious metal catalysts, where superior catalysis has been observed in NPM catalysts such as perovskites,[6] spinels[7] and metal oxides.[8] However, these OER catalysts typically

[a]*Department of Chemistry, School of Engineering, Dayananda Sagar University, Bengaluru, India. E-mail: ashok022@gmail.com*

[b]*Faculty of Science and Engineering, Manchester Metropolitan University, Chester Street, M1 5GD, UK. E-mail: c.banks@mmu.ac.uk; Tel: +44 (0)1612471196*

[c]*Manchester Fuel Cell Innovation Centre, Manchester Metropolitan University, Chester Street, Manchester M1 5GD, UK*

[d]*Department of Chemistry, SVM Arts, Science and Commerce College, Ilkal 587125, India*

[e]*Department of Chemistry, RV College of Engineering, Bengaluru 590059, India*

† Electronic supplementary information (ESI) available. See DOI: 10.1039/d0ra10597j

require complex synthesis protocols, which limits their scalability within commercial electrolysis, thus the research into mass producible NPM based catalysts is imperative to the advancement of electrolyser technologies.

In the search for NPM OER electrocatalysts, researchers have focused on a range of abundant and cheap oxides, such as nickel, iron, manganese and cobalt.[9–15] The OER is generally catalysed by a metal oxide rather than a pure metal, with the mechanism different for oxides with different surface morphologies. It has been reported that the OER activity of metal oxides follows the trend of $NiO_x > CoO_x > FeO_x > MnO_x$,[16,17] with Ni based oxides reported to exhibit the most promising OER catalysis owing to their high intrinsic activity;[18,19] In exemplifying the case of a metal surface *versus* a metal oxide, Babar *et al.*[17] explored a thermally oxidized porous NiO supported on nickel foam (NF) in 1.0 M KOH towards the OER. The NiO/NF annealed at 400 °C required an overpotential of 310 mV to reach +10 mA cm^{-2}, compared to the bare NF, which exhibited an overpotential of 400 mV. The beneficial OER performance exhibited by NiO/NF is attributed to the formation of porous NiO within the NF substrate, which provides a large electrochemical surface area with a larger number of exposed active sites, therefore an enhanced signal output. On the other hand, various studies have reported that NiO possesses a large bandgap and therefore poor electrical conductivity, resulting in limited kinetics. This can be mitigated by alloying NiO with metallic Ni, where the bandgap associated with NiO is reduced by the addition of Ni, thus increasing electrochemical charge transfer rates.[20,21]

The synthesis of Ni/NiO composites have previously been reported in literature; however, these studies have failed to control the quantity and homogeneous distribution of Ni within the NiO matrix.[21–25] Zhou *et al.*[26] reported a Ni/NiO composite embedded in graphitic carbon (Ni–NiO/C) that displayed excellent activity and stability as a water splitting catalyst in alkaline conditions. However, the Ni–NiO/C composite was synthesised using complex experimental conditions, involving the hydrothermal growth of nickel organic frameworks on nickel foam at 120 °C for 36 h, followed by calcination at 600 °C for 2 h within an inert atmosphere. The development of scalable, rapid and facile methodologies to synthesise Ni/NiO is essential if OER catalysts are to be utilised within commercial AEM electrolysers. Consequently, we report a facile synthesis methodology encompassing a solution combustion method, which allows for the content of Ni to be controlled that meets the requirements specified above for the large-scale production of Ni/NiO nanocomposites.

2. Experimental section

2.1. Chemicals

All chemicals utilised within this study were of an analytical grade and were used as received without any further purification. All solutions were prepared with deionised water of resistivity not less than 18.2 MΩ cm. Nickel(II) nitrate hexahydrate (Ni(NO$_3$)$_2$·6H$_2$O) and citric acid (C$_6$H$_8$O$_7$) were purchased from SD Fine Chemicals Ltd India. Electrochemical

measurements were performed in 1.0 M KOH, which was of the highest possible purity from SD Fine Chemicals Ltd India (99.999%, double distilled for trace metal analysis). It has to be noted that the testing of the NiO composites needs to be performed in ultra-pure, metallic impurity free alkaline solutions to avoid giving rise to false observation of enhanced OER performance from metallic impurities.[27]

2.2. Synthesis of the Ni/NiO nanocomposites

Previous studies have reported that the phase/composition of the products prepared *via* solution combustion synthesis are controlled by two factors; the selection of fuel and the oxidant-to-fuel ratio. These factors have a significant effect on the exothermicity and combustion environment of the reaction, thus influence phase formation. Herein, a simple and controlled one-step facile solution based methodology, based upon a citrate–nitrate decomposition is utilised to synthesize Ni/NiO nanocomposites. In this novel approach, Ni(NO$_3$)$_2$·6H$_2$O is used as the oxidant and C$_6$H$_8$O$_7$ as the fuel and complexing agent. In a typical reaction, 0.50 g of Ni(NO$_3$)$_2$·6H$_2$O is dissolved into 10 mL of deionized water under magnetic stirring, followed by the addition of 0.20 g C$_6$H$_8$O$_7$ and further stirred for another 5 minutes. The beaker containing the resultant product, in solution, was transferred into a preheated muffle furnace maintaining a temperature of 500 °C for different time intervals, namely, 4 min, 30 min, 2 hours and 8 hours, which is utilised to control the Ni content within the Ni/NiO nanocomposites. Finally, the obtained Ni/NiO nanocomposites are ground into a fine powder prior to drop casting onto the working area of SPEs (see below) for electrochemical investigations.

2.3. Electrochemical measurements

Electrochemical measurements were performed using a typical three-electrode setup at room temperature in 1.0 M KOH solution. A Biologic SP-150™ (France) potentiostat was used to carry out electrochemical measurements using a three-electrode configuration. The working electrodes used in this study are screen-printed graphitic macroelectrodes (with the dimensions of 41 mm long × 7 mm wide), which comprise a three electrode configuration with a 3.1 mm graphite working electrode, a graphite counter and an Ag/AgCl pseudo-reference electrode. These SPEs are fabricated in-house with appropriate stencil designs to achieve a 3.1 mm diameter working electrode respectively, using a microDEK 1760RS screen-printing machine (DEK, Weymouth, UK). Firstly, a carbon-graphite ink formulation (Product Code: C2000802P2; Gwent Electronic Materials Ltd, UK) is printed onto a polyester (Autostat, 250 micron thickness) substrate. This layer is then cured in a fan oven at 60 degrees Celsius for 30 minutes. Finally, a dielectric paste (Product code: D2070423D5; Gwent Electronic Materials Ltd, UK) was then printed onto the polyester substrate to cover the connections. After curing at 60 degrees Celsius for 30 minutes, the screen-printed electrodes are ready to be used. The reproducibility of the batch of screen-printed electrode were found to correspond to less than 4.5% RSD towards the redox

probe, $[Ru(NH_3)]^{2+/3+}/0.1$ M KCl. Edge connectors were used to connect the potentiostat connections to the SPEs.[28] The SPEs are used either "as-is", *i.e.* bare/unmodified or drop-coated with the fabricated (see above) Ni/NiO nanocomposites. The Nernst equation was used to convert an Ag/AgCl reference electrode to the reversible hydrogen electrode (RHE): $E_{RHE} = E_{Ag/AgCl} + 0.059\text{pH} + 0.1976$ V (at 25 °C).

2.4. Fabrication of the Ni/NiO screen-printed graphitic macroelectrodes (SPEs)

The use of SPEs as a substrate is advantageous compared to the other carbon based electrodes, due to their ability to be mass-produced but yet exhibit remarkable stability with regards to their electrochemical signal output.[29,30] In order to fabricate the bare/unmodified SPEs used within this study, a 3.0 mg mL^{-1} homogenous dispersion of the synthesized Ni/NiO nano-composite, described above, was dispersed into water and sonicated for 30 minutes with 10 μL of the suspension drop cast onto the working area of an SPE. All SPEs used within this study exhibit a catalyst loading of 0.004 mg cm^{-2} and were dried under infra-red light. This constant catalyst loading allows direct comparison between the different Ni/NiO nano-composites explored in this study and allows comparison with that of the academic literature. This relatively low surface electrode modification (catalyst loading) also ensures that a porous surface is avoided, such that the observed voltam-metric response is due to the electrocatalyst itself rather than a simple change in mass transport compared to a bare/unmodified electrode (*i.e.* linear diffusion → thin-layer behav-iour), which has been led to previously work misinterpret as electrocatalysis. The resultant Ni/NiO SPEs are denoted throughout as: 4m-Ni/NiO SPE, 30m-Ni/NiO SPE, 2h-Ni/NiO SPE and 8h-Ni/NiO SPE, indicating the time of reaction of each Ni/NiO nanocomposite (see above) utilised.

3. Results and discussion

3.1. Physicochemical characterisation of the Ni/NiO nanocomposites

As described in the experiment section, a unique and facile solution combustion synthetic methodology is reported in order to produce and explore the effect of the Ni/NiO ratio upon the oxygen evolution reaction (OER). Prior to electrochemical exploration of the Ni/NiO nanocomposites towards the OER, a thorough physicochemical characterisation was performed using scanning electron microscopy (SEM), X-ray photoelectron spectroscopy (XPS) and X-ray diffraction (XRD).

XRD was utilised to assess the crystallinity of the synthesised Ni/NiO nanocomposites. The XRD patterns of the Ni/NiO nanocomposites annealed at 500 °C for 4 min, 30 min, 2 hours and 8 hours are displayed within Fig. 1. The XRD stan-dards for Ni (JCPDS 65-2865), exhibits diffraction peaks at 2θ values of 45.1°, 52.0° and 76.4° corresponding to the single crystal faces (111), (200) and (220), while the NiO standard (JCPDS 65-5745) relates to 2θ values of 37.2°, 43.2°, 62.8°, 75.6° and 79.4° corresponding to the single crystal faces (111), (200),
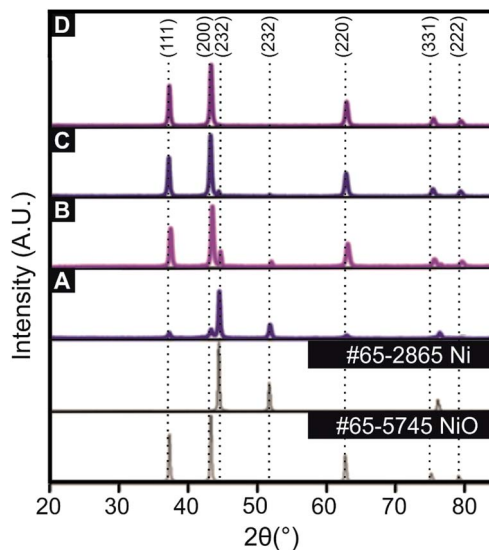

Fig. 1 XRD patterns of the Ni/NiO nanocomposites which have been annealed at 500 °C for: (A) 4 min (B) 30 min (C) 2 hours and (D) 8 hours. Comparisons are made with the Ni and NiO JCPDS XRD standards.

(220), (311) and (222). Analysis of the XRD peak areas, using the 43.2° (200), NiO and 45.1° (111), Ni single crystal faces as a function of annealing time reveals the following ratios: 0.071 : 0.307; 0.374 : 0.499; 0.372 : 0.011; 0.368 : 0 for 4 min, 30 min, 2 hours and 8 hours respectively. In comparison of the various XRD patterns presented in Fig. 1, it is clear that an annealing time of 4 min results in a sample that contains a small amount of NiO, which is predominantly comprised of Ni. As the annealing time is increased the Ni/NiO material transforms to one where the NiO predominates over the Ni content, which is readily achieved within 2 hours. Note that the (111) diffraction peak decreases as the annealing time in increased, which is absent in the longest annealing time of 8 hours, which has resulted in a material comprised purely of NiO. The surface morphology of an electrocatalyst significantly affects the electrochemical performance towards water split-ting, which was visually assessed using SEM. ESI Fig. S1† shows SEM images of the Ni/NiO nanocomposites where it is clear that as the annealing time increases, agglomeration of the fine Ni/NiO particles of size 30–40 nm, also increases. Such agglomer-ation will reduce the accessible surface area for electrocatalytic sites to be assessable, but it is the nanocomposites composition that is more dominant; electrochemical performance and ToF as evaluated later will give more insights.

XPS was also utilised, with Fig. 2(A) showing the XPS survey spectrum confirming the presence of Ni, O, and C, where the carbon content is a result of the adsorbed carbon dioxide or small amount of carbon remaining from the fabrication process (fuel), as detailed in the experimental section. Also shown is the key Ni 2s and Ni 2p regions. Fig. 2(B) shows the high-resolution XPS spectra of the different Ni/NiO nanocomposites, which exhibits a characteristic XPS spectra for NiO displaying a multiplet-split Ni 2p$_{3/2}$ at 853.6 and 855.4 eV, and a Ni 2p$_{3/2}$ satellite at 860.6 eV with a multiplet-split. Additionally a Ni 2p$_{3/2}$
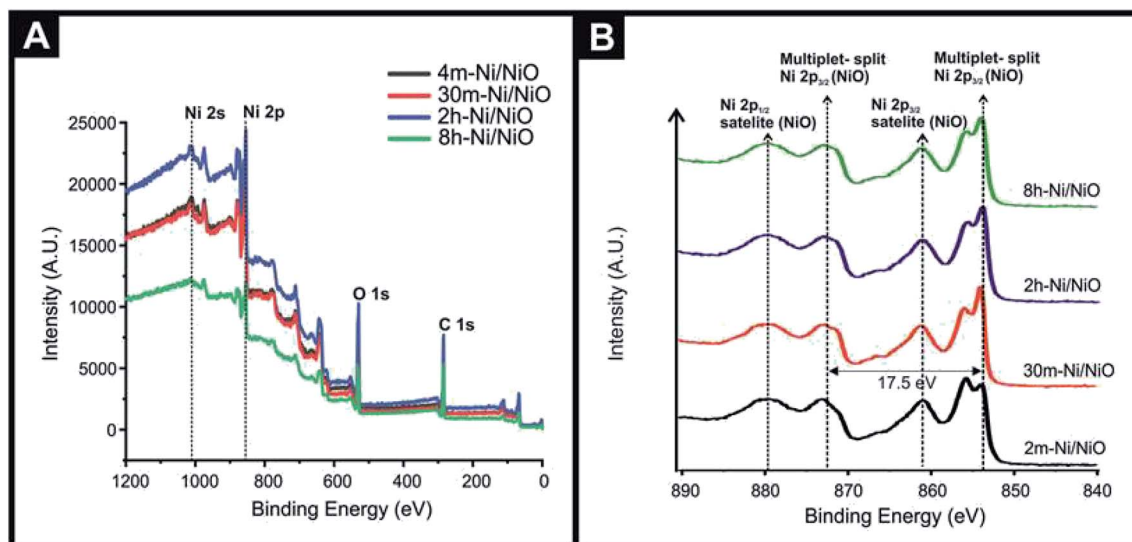
Fig. 2 (A) High resolution XPS survey of the Ni/NiO nanocomposites; intensity (×10) (A.U.) *vs.* binding energy (eV). (B) High resolution XPS spectra of the Ni 2p regions within the Ni/NiO nanocomposites annealed for 4 min, 30 min, 2 hours and 8 hours.

at 871.1 eV and Ni $2p_{1/2}$ satellite at 879.9 eV is also observable, which is agreement with previous studies.[31] It is worth noting that the Ni(0) peak is not readily identified in the XPS spectra, whilst it is identified in the XRD patterns. This may be due to the formation of NiO upon the Ni particles or where the Ni is embedded within/throughout the NiO, also worth noting is the different depth penetration profiles of the two techniques and also that the XPS binding energy of Ni metal, NiO are very close.

3.2. Electrochemical performance of the Ni/NiO SPEs towards the OER

The various Ni/NiO nanocomposites following physicochemical characterisation are next electrochemically explored towards the OER within ultrapure 1.0 M KOH. Fig. 3(A) displays typical linear sweep voltammograms obtained for the 4m-Ni/NiO SPE, 30m-Ni/NiO SPE, 2h-Ni/NiO SPE and 8h-Ni/NiO SPE, benchmarked against a bare/unmodified SPE. The insert of Fig. 3(A) displays an electrochemical oxidation peak, followed by the onset of the OER at higher anodic potentials. This initial voltammetric feature is likely due to the electrochemical oxidation process, $Ni^{2+/3+}$, which can be described by: $NiO + OH^- \rightarrow NiOOH + e^-$ and at higher potentials the OER process occurs, which is consistent with literature reports.[32–34]

The voltammetric responses in terms of overpotential, for the Ni/NiO nanocomposites, towards the OER were benchmarked at +10 mA cm^{-2}, as is common within the literature. The potentials required to reach +10 mA cm^{-2} were found to be 420 (1.65 *vs.* RHE), 279 (1.50 *vs.* RHE), 254 (1.48 *vs.* RHE), 231 (1.46 *vs.* RHE) and 288 mV (1.51 *vs.* RHE) for the bare/unmodified SPE, 4m-Ni/NiO SPE, 30m-Ni/NiO SPE, 2h-Ni/NiO SPE and 8h-Ni/NiO SPE, respectively. It is evident that as the annealing time is increased, the voltammetric response reduces in overpotential, with the 2h-Ni/NiO SPE giving rise to the optimal response towards the OER. Of interest the 30m-Ni/NiO

SPE shows an oxidation peak of quite higher intensity and shifted towards higher potentials compared to the most performant sample, the 2h-Ni/NiO SPE. This is likely due to composition still being dominate towards NiO. Note that these results are favourable, if not better than other nickel based composites, as overviewed in Table 1. A notable percentage increase in achievable current density of 134% is observed in the 2h-Ni/NiO SPE in comparison to a bare/unmodified SPE. The 30m-Ni/NiO SPE and 2h-Ni/NiO SPE display high achievable current densities of between 160–175 mA cm^{-2}, which is due to a high content of conductive metallic Ni atoms. It is interesting to note that increasing the annealing time up to 8 h results in a voltammetric response displaying less beneficial electrocatalytic activity towards the OER, which might be on first sight counter-intuitive. This decrease in activity can be explained by inspection of the physicochemical analysis presented above, particularly the XRD patterns (see Fig. 1), and the electrochemical data reported in Fig. 3, it is evident that a pure NiO phase is a poor material towards the OER. This is consistent with literature reports and the introduction of metallic Ni atoms reduce the bandgap associated with NiO, thus increase the charge transfer rate between electrode and electrolyte.[35]

3.3. Tafel analysis

The Tafel slope is routinely employed in the analysis of potential new OER catalysts. Material scientists spend a great deal of time and effort making and characterising new potential OER materials with significant emphasis applied to the physicochemical and electrochemical analysis of the new material. Tafel analysis is, however, routinely applied, without further analysis and respect to the potential underlying electrochemical mechanism. The reason for this is that the academic literature reports many versions of the Butler–Volmer equation and corresponding Tafel analysis, which to non-specialists can be, on first sight overwhelming. As such, the Tafel equation is often
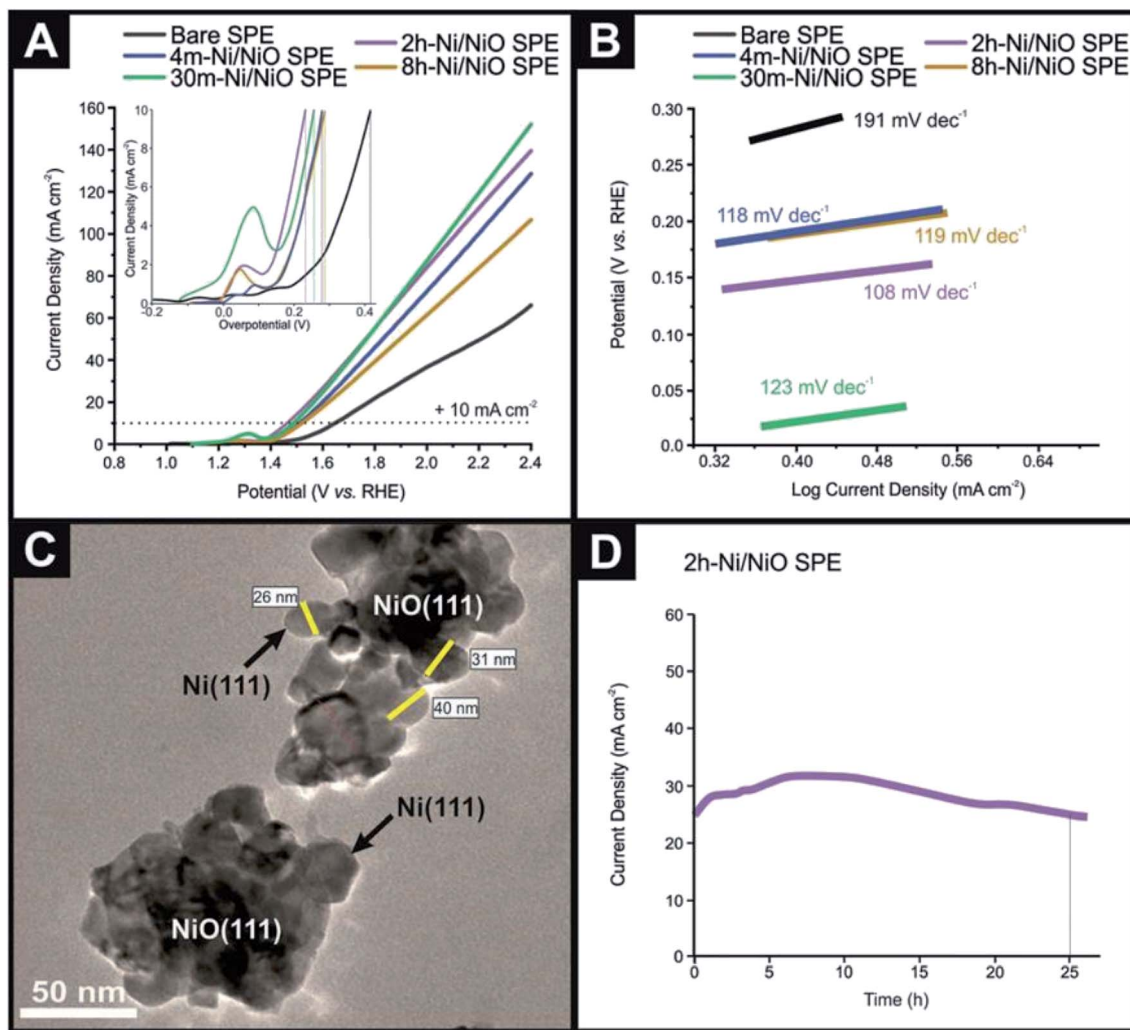
Fig. 3 (A) Typical linear sweep voltammetry of a bare/unmodified SPE in 1.0 M KOH as well as the 4m-Ni/NiO SPE, 30m-Ni/NiO SPE, 2h-Ni/NiO SPE and 8h-Ni/NiO SPE, exhibiting the onset potential of the OER. Scan rate: 5 mV s^{-1}. (B) Tafel analysis: overpotential (*vs.* overpotential) *vs.* log$_{10}$ (current density) (j mA cm^{-2}) for the faradaic region from (A). (C) TEM image of the 2h-Ni/NiO nanocomposite. (D) Chronoamperometric response of the 2h-Ni/NiO SPE held at +231 mV for 26 h.

used to solely report the Tafel slope, which is then used to benchmark a particular catalytic materials against others reported in the academic literature. We seek here to help the field progress by coherently summarising how Tafel analysis can be employed to provide qualitative, yet useful, information upon the material being studied towards the OER. We note that the analysis below is not new,[36] but we provide a summary below to help those new to the field developing new OER materials. We first consider a simple one-step, *n*-electron transfer process:

$$A + ne^- \rightleftarrows B$$
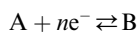
with such kinetics for this process are described by the classic Butler–Volmer equation,[37–43] assuming $n = 1$:

$$I = I_0 \left(\exp\left(\frac{(1-\beta)F\left(E - E_f^0\right)}{RT} \right) - \exp\left(\frac{\beta F\left(E - E_f^0\right)}{RT} \right) \right)$$

(1.1)

where I is the overall current density, I_0 is the equilibrium exchange-current density, F is the Faraday constant, β is the electron transfer symmetry factor, E_f^0 is the formal potential of redox couple, where $E - E_f^0$ measures the potential applied to the working electrode (E) relative to the formal potential of the electron transfer process, R is the universal gas constant and T is temperature. Within the academic literature, there are many forms of the famous Butler–Volmer. For example, noting that: $\alpha + \beta = 1$. Eqn (1.1) can also be presented as follows:

$$I = I_0 \left(\exp\left(\frac{-\alpha F\left(E - E_f^0\right)}{RT} \right) - \exp\left(\frac{(1-\alpha)F\left(E - E_f^0\right)}{RT} \right) \right)$$

(1.2)

Under extreme potential, *e.g.* $E \gg E_f^0$ or $E \ll E_f^0$, the eqn (1.2) can be simplified where one term or another is neglected. In the case of an electrochemical reduction, *i.e.*.

Paper

Table 1 Summary of current literature reporting to nickel based OER electrocatalysts[a]

Catalyst	Supporting electrode	Electrolyte	Stability	Deposition technique	Catalyst loading	OER overpotential at 10 mA cm^{-2} (mV vs. RHE)	Tafel value (mV dec^{-1})	Ref.
$NiCo_2O_4/CoO$	SPEs	1.0 M KOH	10 h at +700 mV (vs. Ag/AgCl)	Drop-cast	0.53 mg cm^{-2}	323	118	58
$Ni_{90}Fe_{10}$	AAO	1.0 M KOH	24 h at +400 mA cm^{-2} (vs. RHE)	Electrodeposition	—	236	45	59
Ni	AAO	1.0 M KOH	—	Electrodeposition	—	405	117	59
NiO	NF	1.0 M KOH	12 h at +153 mV (vs. RHE)	Drop casting	—	356	77	60
NiO nanowalls	Quartz/Ti/Au	1.0 M KOH	—	Sputtering deposition	—	345	48	56
Ni/NiO	CP	1.0 M KOH	13.8 h at +158 mV (vs. RHE)	Drop casting	—	353	97	61
Ni_3S_2/NiS	GCE	1.0 M KOH	15 h at +10 mA cm^{-2} (vs. RHE)	Drop cast	0.20 mg cm^{-2}	298	58	62
$NiO@NiMoO_4$	NF	1.0 M KOH	12 h at +10 mA cm^{-2} (vs. RHE)	Chemical growth	1.40 mg cm^{-2}	280	32	63
NiO nanosheets	NF	1.0 M KOH	12 h at +10 mA cm^{-2} (vs. RHE)	Chemical growth	0.30 mg cm^{-2}	340	97	63
NF	N/A	1.0 M KOH	12 h at +10 mA cm^{-2} (vs. RHE)	N/A	N/A	340	109	63
rGO/Ni_2P	GCE	1.0 M KOH	30h at + 10 mA cm^{-2} (vs. RHE)	Drop cast	0.10 mg cm^{-2}	283	44	64
NiO_x–Fe	NF	1.0 M KOH	18 h at +10 mA cm^{-2} (vs. RHE)	Chemical growth	0.014 mg cm^{-2}	266	36	11
$P–NiFe_2O_4$	CC	1.0 M KOH	50 h at +10 mA cm^{-2} (vs. RHE)	Chemical vapour deposition	—	231	49	65
$Ni_{32}Fe$	GC	1.0 M KOH	50 h at +10 mA cm^{-2} (vs. RHE)	Drop casting	0.12 mg cm^{-2}	291	58	66
$NiCeO_x$	GCE	1.0 M KOH	200 h at +10 mA cm^{-2} (vs. RHE)	Chemical growth	—	295	66	67
NiO–NiFe–LDH	NF	1.0 M KOH	16.5 h at +10 mA cm^{-2} (vs. RHE)	Chemical growth	—	265	72	68
$Ni–Ni(OH)_2$	CF	1.0 M KOH	24h at + 10 mA cm^{-2} (vs. RHE	Electrodeposition	—	290	97	69
Ni/NiO_x	NF	1.0 M KOH	5.5 h at +500 mV (vs. SCE)	Chemical growth	—	390	70	70
Ni/NiO	NF	1.0 M KOH	30 h at +10 mA cm^{-2} (vs. RHE)	Drop casting	0.51 mg cm^{-2}	295	74	26
4m-Ni/NiO	SPEs	1.0 M KOH	—	Drop casting	0.004 mg cm^{-2}	279	118	This work
30m-Ni/NiO	SPEs	1.0 M KOH	—	Drop casting	0.004 mg cm^{-2}	254	123	This work
2h-Ni/NiO	SPEs	1.0 M KOH	26 h at +700 mV (vs. RHE)	Drop casting	0.004 mg cm^{-2}	231	108	This work
8h-Ni/NiO	SPEs	1.0 M KOH	—	Drop casting	0.004 mg cm^{-2}	288	119	This work

[a] Key: SPEs – screen-printed electrodes; RHE – reversible hydrogen electrode; AAO – anodic aluminium oxide (AAO) membrane; GCE – glassy carbon electrode; GC – graphitic carbon; NF – nickel Foam; rGO – reduced Graphene oxide; AC – acid cleaned; CC – carbon cloth; LDH – layer double hydroxide; CP – carbon fiber paper; CF – copper foil; - = not reported.

$A + e^- \rightarrow B$, eqn (1.2) becomes:[39]

$$I = I_0\left(\exp\left(\frac{-\alpha F\left(E - E_f^0\right)}{RT}\right)\right) \quad (1.3)$$

while for in the case of an electrochemical oxidation, i.e. $B - e^- \rightarrow A$, eqn (1.2) becomes:

$$I = I_0\left(\exp\left(\frac{(1 - \alpha)F\left(E - E_f^0\right)}{RT}\right)\right) \quad (1.4)$$

The corresponding Tafel[44–46] equations are then, from eqn (1.3) and (1.4):

$$\frac{\partial \log_{10} I}{\partial \left(E - E_f^0 \right)} = -\frac{\alpha F}{2.303 RT} + \log_{10} I_0 \tag{1.5}$$

$$\frac{\partial \log_{10} I}{\partial \left(E - E_f^0 \right)} = \frac{(1 - \alpha) F}{2.303 RT} + \log_{10} I_0 \tag{1.6}$$

Experimentally, and historically, the analysis of Tafel slopes are plotted as $(E - E_f^0)$ *vs.* $\log_{10} I$ due to the way they were originally measured, *i.e.* galvanostatic rather than potentiostatic, thus we re-state (1.5) and (1.6) as the following Tafel equations:
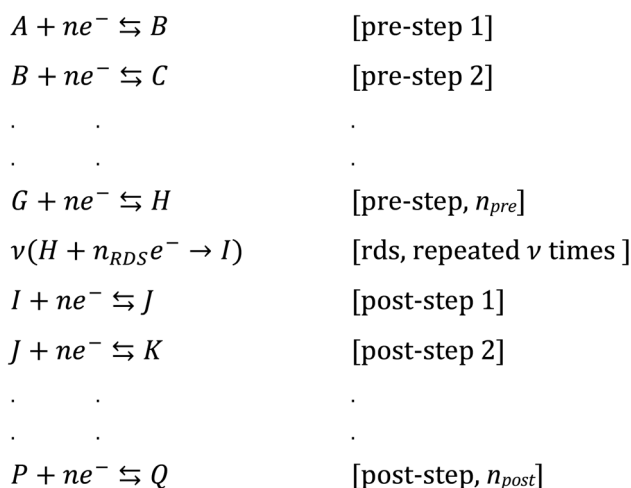
$$\frac{\partial \left(E - E_f^0 \right)}{\partial \log_{10} I} = -\frac{2.303 RT}{\alpha F} \tag{1.7}$$

$$\frac{\partial \left(E - E_f^0 \right)}{\partial \log_{10} I} = \frac{2.303 RT}{(1 - \alpha) F} \tag{1.8}$$

Note that all the above is for a simple one-step, one-electron transfer process, which is the most commonly reported in the academic literature. However, multi-step electrochemical processes, such as that encountered in the OER, as explored in this paper, require a different approach. The Butler–Volmer equation can be modified for a multi-step overall electrochemical reaction process, which comprises electron transfer steps in addition to the rate determining step:[36]

$$I = I_0 \left(\exp\left(\frac{\alpha_{\text{cathode}} F \left(E - E_f^0 \right)}{RT} \right) - \exp\left(\frac{\alpha_{\text{anode}} F \left(E - E_f^0 \right)}{RT} \right) \right) \tag{1.9}$$

Now, let us consider some general electrochemical processes that may be encountered, such as in the OER, in determining a reaction mechanism where Tafel analysis is routinely utilised. If we consider a multi-step reaction, $A + ne^- \rightarrow Q$, which has the following pre-steps:

$A + ne^- \leftrightharpoons B$	[pre-step 1]
$B + ne^- \leftrightharpoons C$	[pre-step 2]
. .	.
. .	.
$G + ne^- \leftrightharpoons H$	[pre-step, n_{pre}]
$v(H + n_{RDS} e^- \rightarrow I)$	[rds, repeated v times]
$I + ne^- \leftrightharpoons J$	[post-step 1]
$J + ne^- \leftrightharpoons K$	[post-step 2]
. .	.
. .	.
$P + ne^- \leftrightharpoons Q$	[post-step, n_{post}]

In this approach, we define n_{pre} to be the number of electrons transferred before the rate-determining step (rds). n_{post} is the number of electrons transferred after the rate-determining step. n_{RDS} is defined as the number of electrons transferred in the rate-determining step and v the stoichiometric number is the number of times the rate-determining step occurs. Note that the total number of electrons, n, in the overall electrode reaction is given by: $n = n_{\text{pre}} + n_{\text{post}} + n_{\text{RDS}}$. Thus, the overall transfer coefficients can be expressed as: $\alpha_{\text{cathode}} = \frac{n_{\text{pre}}}{v} + n_{\text{RDS}}\beta$ where α_{cathode} is the transfer coefficient of the overall forward/anodic reaction, n_{pre} is the number of electrons take up by the electrode before the rds and n_{RDS} is the number of electrons involved in the rate-determining step. Conversely: $\alpha_{\text{anode}} = \frac{n_{\text{post}}}{v} + n_{\text{RDS}}(1 - \beta)$ where α_{anode} is the transfer coefficient of the overall backward/cathodic reaction, leading to:

$$I = I_0 \left(\exp\left(\frac{\left(\frac{n_{\text{pre}}}{v} + n_{\text{RDS}}\beta \right) F \left(E - E_f^0 \right)}{RT} \right) \right.$$
$$\left. - \exp\left(\frac{\left(\frac{n_{\text{post}}}{v} + n_{\text{RDS}}(1 - \beta) \right) F \left(E - E_f^0 \right)}{RT} \right) \right) \tag{1.10}$$

Noting that $\alpha_{\text{cathode}} + \alpha_{\text{anode}} = n/v$ where the rds occurs v times in the electrode reaction. A full derivation is presented by Bockris and Reddy,[36] and later Fletcher[47] but summarised here for the convenience for material scientists developing new OER electrode materials. We next consider some scenarios, to elaborate on the above information. The above is written for an electrochemical reduction/cathodic process, *i.e.* $A + ne^- \rightleftarrows B$, but is applicable for an oxidation/anodic process. Thus if we consider the case of the OER, an anodic process, *i.e.* $A - ne^- \rightarrow B$, we should consider the following:

$$I = I_0 \left(\exp\left(\frac{\left(\frac{n_{\text{post}}}{v} + n_{\text{RDS}}(1 - \beta) \right) F \left(E - E_f^0 \right)}{RT} \right) \right) \tag{1.11}$$

If we now consider some scenarios, for the electrochemical process: $A - ne^- \rightarrow B$, which is considered to be the rate-determining step, it follows from above that we use: $\frac{\partial (E - E_f^0)}{\partial \log_{10} I} = \frac{2.303 RT}{\frac{n_{\text{post}}}{v} + n_{\text{RDS}}(1 - \beta) F}$, where, $v = 1$; $n_{\text{post}} = 0$; $n_{\text{RDS}} = 1$; $\beta = 0.5$ and assuming $T = 298$ K, F is 96 485.3; $R = 8.31$, a Tafel slope of 118 mV decade^{-1} should be experimentally observed. This is known to be the classical result for a single-step one-electron transfer processes. In practice, values are not always precisely 118 mV due to experimental errors. Table 2 overviews a range of multi-step electrochemical mechanisms and the predicted Tafel plots using the notation of Testa and Reinmuth[48] (where E is an electrochemical step, C is a chemical step *etc.*); however, the above approach should allow most, if not all, possible mechanisms encountered in such processes such as the OER. Note that while Tafel analysis and that of Table 2 provides more evidence of the
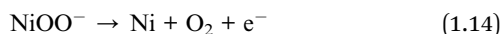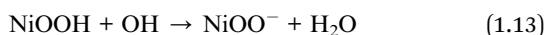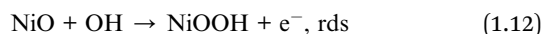
Table 2 Overview of various multi-step electrochemical mechanisms and their corresponding predicted Tafel slope for anodic processes, such as those observed in the OER

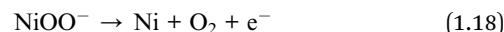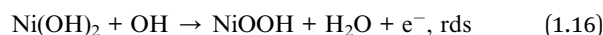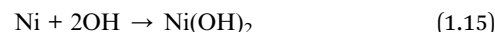| Electrochemical Mechanism		Tafel slope (mV decade^{-1})
E_{rds}	$A - ne- \rightarrow B$	118
$E_{rds}C$	$A - ne^- \rightleftarrows B$	118
	$B \rightarrow C$	
$E_{rds}CE$	$A - ne^- \rightleftarrows B$	118
	$B \rightarrow C$	
	$C - ne^- \rightleftarrows D$	
EC_{rds}	$A - ne^- \rightleftarrows B$	60
	$B \rightarrow C$	
$EC_{rds}E$	$A - ne^- \rightleftarrows B$	60
	$B \rightarrow C$	
	$C - ne^- \rightleftarrows D$	
ECE_{rds}	$A - ne^- \rightleftarrows B$	40
	$B \rightarrow C$	
	$C - ne^- \rightleftarrows D$	
EEC_{rds}	$A - ne^- \rightleftarrows B$	30
	$B - ne^- \rightleftarrows C$	
	$C \rightarrow D$	
$EEEC_{rds}$	$A - ne^- \rightleftarrows B$	20
	$B - ne^- \rightleftarrows C$	
	$C - ne^- \rightleftarrows D$	
	$D \rightarrow E$	

overall electrochemical mechanism, further insights will be needed from physiochemical analysis and/or *in situ* measurements to provide an unambiguous determination.

Returning to the voltammetric responses presented within Fig. 3, Tafel analysis was performed (Fig. 3(B)) with the bare SPE, 4m-Ni/NiO SPE, 30m-Ni/NiO SPE, 2h-Ni/NiO SPE and 8h-Ni/NiO SPE exhibiting Tafel values (slopes) of 191, 118, 123, 108 and 119 mV dec^{-1}, respectively. Using a recently updated Pourbaix diagram for Nickel,[49] and noting that the XPS analysis indicated that the surface morphology is comprised of NiO, which will be the major component exposed at the interfacial surface, while the Ni is embedded through the NiO samples, the underlying electrochemical mechanism, as observed in Fig. 3, is tentatively proposed as follows:

$$NiO + OH \rightarrow NiOOH + e^-, \text{ rds} \tag{1.12}$$

$$NiOOH + OH \rightarrow NiOO^- + H_2O \tag{1.13}$$

$$NiOO^- \rightarrow Ni + O_2 + e^- \tag{1.14}$$

where the first step (1.12) is the rate determining step (rds), followed by a fast chemical (1.13) and fast electrochemical step (1.14) which is in the notation: $E_{rds}CE$. Note that experiential evidence of $NiOO^-$ in the OER has been provided.[50] Using eqn (1.11), the multistep electrochemical reaction proposed is 118 mV decade^{-1}, which is in agreement with the Tafel values measured experimentally, noting the errors imposed from experimentation. How do we know that the observed Tafel is close to that of the proposed mechanism above? Recourse to Table 1 reveals, that there are two other possibilities, which are of an $EC_{rds}E$ where the C step is the rds or that of ECE_{rds}, where

the final electrochemical step is the rds. In the case of $EC_{rds}E$ and ECE_{rds}, the predicted Tafel slope is 60 and 40 mV decade^{-1}, respectively (see above and Table 2). Even accounting for experimental error, the closet fits our proposed $E_{rds}CE$ mechanism. The above proposed multistep reaction mechanism (*i.e.* eqn (1.12)–(1.14) is along similar lines reported for other nickel based systems.[24,51] We note that *in situ* physicochemical analysis would be needed to unambiguously determine the underlying reaction mechanism. However, we now how, if the reaction mechanism is potentially favourable the production of Ni metal (see eqn (1.14)). Thus, there is another mechanism that is likely in play:

$$Ni + 2OH \rightarrow Ni(OH)_2 \tag{1.15}$$

$$Ni(OH)_2 + OH \rightarrow NiOOH + H_2O + e^-, \text{ rds} \tag{1.16}$$

$$NiOOH + OH \rightarrow NiOO^- + H_2O \tag{1.17}$$

$$NiOO^- \rightarrow Ni + O_2 + e^- \tag{1.18}$$

which again, is $CE_{rds}CE$. Likely both are in operation over the course of the OER, but it is yet unknown which is the dominant reaction mechanism at any one point, for example, over long extended period of the OER, *e.g.* chronoamperometry experiment shown later. The Ni/NiO system applied to the OER is definitely worthy of more electrochemical mechanistic investigation.

Further characterisation of the 2h-Ni/NiO nanocomposite was performed, with Fig. 3(B) showing a transition electron microscope (TEM) image indicating the Ni/NiO particles are in the range of 25–45 nm. The particles exhibit a large surface area with irregular morphologies where the observed OER kinetics, enhanced by the formation of the Ni–NiO hetero-structures are due to the synergistic effect between NiO and metallic Ni, where the surface layer of NiO exhibits a high number of active sites. These active sites allow oxygen to readily form, and the surrounding metallic Ni atoms serve as short diffusion pathways and channels for rapid electron transport.[52,53]

The electrochemically active surface area (ECSA) was determined by the specific capacitance method, as advocated within the academic literature *via* the following equation: $ECSA = C_d/C_s$ where a literature value of 0.04 mF cm^{-2} is used for C_s, while the value of C_d is determined experimentally. The latter is determined for the various Ni/NiO nanocomposites with cyclic voltammograms recorded in 0.1 M KOH within a non-Faradaic region (*i.e.* 0.04 to 0.15 V (*vs.* Ag/AgCl)) over the range of scan rates from 10 mV s^{-1} to 50 mV s^{-1}; see ESI Fig. S2.† The capacitance of an electrode surface can be determined *via* cyclic voltammetry within a potential window (see ESI Fig. S2†) where no Faradaic reactions occur. ESI Fig. S2† shows typical results where a plot of current *vs.* scan rate, *v* is constructed allowing the capacitance, *C*, of the electrode surface to be deduced from: $I = Cv$. Consequently, ECSA values of 2.5, 19.3, 21.3, 125.0, 8.1 were determined for bare SPE, 4m-Ni/NiO SPE, 30m-Ni/NiO SPE, 2h-Ni/NiO SPE and 8h-Ni/NiO SPE respectively. While these values likely do not reflect the true electrochemical area,

they provide some form of benchmark. The effective resistance, or impedance, of the electrical circuit was measured for the various Ni/NiO SPEs. Electrochemical impedance spectra (EIS) were recorded at an amplitude of 10 mV (vs. RHE) and frequency range 0.1–100 000 Hz in 1.0 M KOH solution (shown in ESI Fig. S3†). The charge transfer resistance (Ω) values of 581.1, 337.7, 325.5, 218.4 and 472.9 Ω are exhibited by the bare SPE, 4m-Ni/NiO SPE, 30m-Ni/NiO SPE, 2h-Ni/NiO SPE and 8h-Ni/NiO SPE, respectively. It is clear that the 2h-Ni/NiO SPE exhibits the lowest charge transfer resistance, which coincides with the water splitting catalysis displayed by the nanocomposites, in regards to the 2h-Ni/NiO SPE exhibiting the fastest charge transfer rate and lowest OER overpotential.

Last, the intrinsic catalytic activity of the Ni/NiO nanocomposites towards the OER was estimated by determining the Turnover Frequency (ToF), which is the number of molecules (e.g. O_2) produce per second per site:

$$\text{ToF}_{\min} = jA_{\text{geo}}/nFm \tag{1.19}$$

where j is the current density at the OER onset potential of each Ni/NiO SPE, A is the geometrical surface area of the working electrode, F is the Faraday constant, n is the number of electrons transferred in the overall electrochemical reaction, usually assumed to be 4 and m is the number of moles of active material (e.g. Ni/NiO) upon the working electrode surface. There are two approaches to determining ToF with subtle differences in how one measures the catalyst, that is $\text{ToF}_{\min}$ and $\text{ToF}_{\max}$ where the former will determine the lower limit of the ToF which involves taking all the catalyst atoms into account via a mass loading, while the latter is the maximum limit of the ToF, which is calculated considering only the number of catalyst atoms on the surface, which can be deduced from the ratio of fraction of catalyst atoms to the overall surface area. Given the inherent difficulties in measuring the surface catalyst atoms, the literature generally opts for $\text{ToF}_{\min}$.

One issues is, where to measure the ToF from, some literature advocates the use of using an overpotential of 100 mV or 350 mV, from which the current density is measured.[54–56] Typically the latter value should be utilised as this will correspond to the correct portion of the cyclic voltammetric profile where the OER is in full operation. Using the current density at 350 mV and determining the number of moles of the Ni/NiO catalyst (molecular weight: 133.385 g mol^{-1}) upon the electrode surface, $\text{ToF}_{\min}$ was deducted to be: 0.00138, 0.00180, 0.0204 and 0.0012 s^{-1} for the 4m-Ni/NiO SPE, 30m-Ni/NiO SPE, 2h-Ni/NiO SPE and 8h-Ni/NiO SPE, respectively. The 2h-Ni/NiO SPE displays the fastest rate of O_2 production and thus exhibits the highest faradaic efficiency. These values are of similar magnitude to that reported for similar nickel systems, but fabricated via different approach but without varying the Ni/NiO ratio[21,57] but an order of magnitude slower than others.[54–56]

3.4. Stability of the Ni/NiO nanocomposites

In order for the Ni/NiO nanocomposites to be suitable for use as an anode within a commercial AEM electrolyser, they must of course exhibit sufficient working stability in alkaline

conditions. Therefore, chronoamperometry was used to assess any degradation in current density as a function of time, using the most promising Ni/NiO nanocomposite. Consequently, the 2h-Ni/NiO SPE in 1.0 M KOH was held at a potential of +231 mV, as shown within Fig. 3(D). It can be readily observed that the current density increases initially and indicating a slight enhancement of the catalytic activity of the Ni/NiO catalyst over the first 7 h. This is commonly observed in such experiments, which is a complex result of electrochemical processes, involving kinetics, mass transport and structural reorganisation due to oxygen evolution; the change in the nickel mechanism as shown above it probably the underlying reason. It is evident that the 2h-Ni/NiO SPE retains 100% of its achievable current density after 26 hours continuous electrolysis, demonstrating promising long-term stability in alkaline conditions. The stability of the 2h-Ni/NiO SPE at highly oxidative potentials is likely a result of a high NiO content as previously demonstrating long-term stability.[17] ESI Fig. S1(E and F)† shows SEM images obtained after the OER process, which indicates no visual morphological modifications induced by the OER activity. Post-OER structural characterisation of the sample, 2h-Ni/NiO SPE, was performed via XRD, the results of which are presented in ESI Fig. S4.† The XRD data obtained for post-OER sample is compared with that of the 2h-Ni/NiO SPE where the XRD pattern of the post-OER sample is visually similar to the fresh 2h-Ni/NiO SPE sample indicating excellent stability and demonstrates the synthesized 2h-Ni/NiO sample is likely to be highly suitable for long-term electrolysis, with potential application in AEM electrolysers.

4. Conclusions

We have explored the application of Ni/NiO nanocomposites, produced via a facile solution combustion method, towards the OER within an alkaline (1.0 KOH) solution and demonstrated, for the first time, that controlling the content ratio of Ni to NiO, by altering annealing times, leads to optimal OER electrocatalytic activity. We suggest future research should focus on the further tuning of the metallic Ni concentration within the NiO matrix to demonstrate excellent long-term activity and stability when deposited onto anion conducting membranes used within anion exchange membrane (AEM) electrolysis.

Conflicts of interest

There are no conflicts to declare.

Acknowledgements

References

1 D. Gielen, F. Boshell, D. Saygin, M. D. Bazilian, N. Wagner and R. Gorini, *Energy Strategy Reviews*, 2019, **24**, 38–50.

2 A. N. Colli, H. H. Girault and A. Battistel, *Materials*, 2019, **12**, 1336.

3 S. S. Dihrab, K. Sopian, M. A. Alghoul and M. Y. Sulaiman, *Renewable Sustainable Energy Rev.*, 2009, **13**, 1663–1668.

4 A. S. Gago, S. A. Ansar, B. Saruhan, U. Schulz, P. Lettenmeier, N. A. Cañas, P. Gazdzicki, T. Morawietz, R. Hiesgen, J. Arnold and K. A. Friedrich, *J. Power Sources*, 2016, **307**, 815–825.

5 Y. Leng, G. Chen, A. J. Mendoza, T. B. Tighe, M. A. Hickner and C.-Y. Wang, *J. Am. Chem. Soc.*, 2012, **134**, 9054–9057.

6 P. Kolla, G. Nasymov, R. Rajappagowda and A. Smirnova, *J. Power Sources*, 2020, **446**, 227234.

7 J. Béjar, L. Álvarez-Contreras, J. Ledesma-García, N. Arjona and L. G. Arriaga, *J. Electroanal. Chem.*, 2019, **847**, 113190.

8 H. Osgood, S. V. Devaguptapu, H. Xu, J. Cho and G. Wu, *Nano Today*, 2016, **11**, 601–625.

9 B. H. R. Suryanto, Y. Wang, R. K. Hocking, W. Adamson and C. Zhao, *Nat. Commun.*, 2019, **10**, 5599.

10 Y. Yan, B. Y. Xia, B. Zhao and X. Wang, *J. Mater. Chem. A*, 2016, **4**, 17587–17603.

11 F. Song, M. M. Busch, B. Lassalle-Kaiser, C.-S. Hsu, E. Petkucheva, M. Bensimon, H. M. Chen, C. Corminboeuf and X. Hu, *ACS Cent. Sci.*, 2019, **5**, 558–568.

12 S. Gupta, A. Yadav, S. Bhartiya, M. K. Singh, A. Miotello, A. Sarkar and N. Patel, *Nanoscale*, 2018, **10**, 8806–8819.

13 X. Deng and H. Tüysüz, *ACS Catal.*, 2014, **4**, 3701–3714.

14 V. S. Kumbhar, H. Lee, J. Lee and K. Lee, *Carbon Resour. Convers.*, 2019, **2**, 242–255.

15 M. M. Najafpour, F. Ebrahimi, M. Abasi and S. M. Hosseini, *Int. J. Hydrogen Energy*, 2016, **41**, 18472–18477.

16 L. Zhuang, L. Ge, Y. Yang, M. Li, Y. Jia, X. Yao and Z. Zhu, *Adv. Mater.*, 2017, **29**, 1606793.

17 P. T. Babar, A. C. Lokhande, M. G. Gang, B. S. Pawar, S. M. Pawar and J. H. Kim, *J. Ind. Eng. Chem.*, 2018, **60**, 493–497.

18 J. Li, J. Li, X. Zhou, Z. Xia, W. Gao, Y. Ma and Y. Qu, *ACS Appl. Mater. Interfaces*, 2016, **8**, 10826–10834.

19 C. Ray, S. C. Lee, B. Jin, A. Kundu, J. H. Park and S. C. Jun, *ACS Sustainable Chem. Eng.*, 2018, **6**, 6146–6156.

20 X. Liu, W. Liu, M. Ko, M. Park, M. G. Kim, P. Oh, S. Chae, S. Park, A. Casimir, G. Wu and J. Cho, *Adv. Funct. Mater.*, 2015, **25**, 5799–5808.

21 M. K. Paliwal and S. K. Meher, *New J. Chem.*, 2020, **44**, 17507–17517.

22 H. Sun, Z. Ma, Y. Qiu, H. Liu and G.-g. Gao, *Small*, 2018, **14**, 1800294.

23 C. Li, J. Hou, Z. Wu, K. Guo, D. Wang, T. Zhai and H. Li, *Sci. China Mater.*, 2017, **60**, 918–928.

24 R. Zhang, H. Wei, W. Si, G. Ou, C. Zhao, M. Song, C. Zhang and H. Wu, *Materials*, 2017, **10**, 15.

25 A. Munir, T. u. Haq, A. Qurashi, H. u. Rehman, A. Ul-Hamid and I. Hussain, *ACS Appl. Energy Mater.*, 2019, **2**, 363–371.

26 W. Zhou, X.-F. Lu, J.-J. Chen, T. Zhou, P.-Q. Liao, M. Wu and G.-R. Li, *ACS Appl. Mater. Interfaces*, 2018, **10**, 38906–38914.

27 D. A. Corrigan, *J. Electrochem. Soc.*, 1987, **134**, 377–384.

28 F. E. Galdino, C. W. Foster, J. A. Bonacin and C. E. Banks, *Anal. Methods*, 2015, **7**, 1208–1214.

29 J. P. Hughes, F. D. Blanco, C. E. Banks and S. J. Rowley-Neale, *RSC Adv.*, 2019, **9**, 25003–25011.

30 S. J. Rowley-Neale, D. A. Brownson, G. C. Smith, D. A. Sawtell, P. J. Kelly and C. E. Banks, *Nanoscale*, 2015, **7**, 18152–18168.

31 A. N. Mansour, *Surf. Sci. Spectra*, 1994, **3**, 231–238.

32 C. Zhang, L. Qian, K. Zhang, S. Yuan, J. Xiao and S. Wang, *J. Mater. Chem. A*, 2015, **3**, 10519–10525.

33 Z. Yue, W. Zhu, Y. Li, Z. Wei, N. Hu, Y. Suo and J. Wang, *Inorg. Chem.*, 2018, **57**, 4693–4698.

34 W. Deng, Y. Liu, Y. Zhang, F. Lu, Q. Chen and X. Ji, *RSC Adv.*, 2012, **2**, 1743–1745.

35 O. Seo, A. Tayal, J. Kim, C. Song, Y. Chen, S. Hiroi, Y. Katsuya, T. Ina, O. Sakata, Y. Ikeya, S. Takano, A. Matsuda and M. Yoshimoto, *Sci. Rep.*, 2019, **9**, 4304.

36 J. O. '. M. Bockris and A. K. N. Reddy, *Modern Electrochemistry*, Plenum, New York, 1973, vol. 2, pp. 991–1017.

37 J. A. V. Butler, *Trans. Faraday Soc.*, 1899, **19**, 729.

38 T. Erdey-Gruz and M. Volmer, *Z. Phys. Chem. A*, 1930, **150**, 203.

39 R. G. Compton and C. E. Banks, *Understanding Voltammetry*, Imperial College Press, London, 2nd edn, 2010, p. 46.

40 T. Erdey-Grúz and M. Volmer, *Z. Phys. Chem. A*, 1930, **150**, 203.

41 J. A. V. Butler, *Trans. Faraday Soc.*, 1932, **28**, 379.

42 J. A. V. Butler, *Trans. Faraday Soc.*, 1924, **19**, 734.

43 J. A. V. Butler, *Trans. Faraday Soc.*, 1924, **19**, 729.

44 J. Tafel, *Z. Phys. Chem.*, 1900, **34**, 187.

45 J. Tafel, *Z. Phys. Chem.*, 1905, **50**, 641.

46 J. Tafel, *Z. Phys. Chem.*, 1906, **12**, 112.

47 S. Fletcher, *J. Solid State Electrochem.*, 2009, **13**, 537–549.

48 A. C. Testa and W. H. Reinmuth, *Anal. Chem.*, 1961, **33**, 1320–1324.

49 L. F. Huang, M. J. Hutchison, R. J. Santucci, J. R. Scully and J. M. Rondinelli, *J. Phys. Chem. C*, 2017, **121**, 9782–9789.

50 S. Lee, K. Banjac, M. Lingenfelder and X. Hu, *Angew. Chem., Int. Ed.*, 2019, **58**, 10295–10299.

51 K. Xu, P. Chen, X. Li, Y. Tong, H. Ding, X. Wu, W. Chu, Z. Peng, C. Wu and Y. Xie, *J. Am. Chem. Soc.*, 2015, **137**, 4119–4125.

52 Y. Zhu, W. Chu, N. Wang, T. Lin, W. Yang, J. Wen and X. S. Zhao, *RSC Adv.*, 2015, **5**, 77958–77964.

53 L. A. García-Cerda, K. M. Bernal-Ramos, S. M. Montemayor, M. A. Quevedo-López, R. Betancourt-Galindo and D. Bueno-Báques, *J. Nanomater.*, 2011, **2011**, 162495.

54 F. E. Sarac Oztuna, T. Beyazay and U. Unal, *J. Phys. Chem. C*, 2019, **123**, 28131–28141.

55 M. Gao, W. Sheng, Z. Zhuang, Q. Fang, S. Gu, J. Jiang and Y. Yan, *J. Am. Chem. Soc.*, 2014, **136**, 7077–7084.

56 S. Cosentino, M. Urso, G. Torrisi, S. Battiato, F. Priolo, A. Terrasi and S. Mirabella, *Mater. Adv.*, 2020, **1**, 1971–1979.

57 C. Mahala and M. Basu, *ACS Omega*, 2017, **2**, 7559–7567.

58 N. Srinivasa, L. Shreenivasa, P. S. Adarakatti, J. P. Hughes, S. J. Rowley-Neale, C. E. Banks and S. Ashoka, *RSC Adv.*, 2019, **9**, 24995–25002.

59 C.-L. Huang, X.-F. Chuah, C.-T. Hsieh and S.-Y. Lu, *ACS Appl. Mater. Interfaces*, 2019, **11**, 24096–24106.

60 X. Ren, Y. Zhai, Q. Zhou, J. Yan and S. Liu, *J. Energy Chem.*, 2020, **50**, 125–134.

61 Y. Li, J. Huang, G. Rao, C. Wu, X. Du, Y. Sun, X. Wang and C. Yang, *Appl. Surf. Sci.*, 2020, **530**, 147192.

62 J. Wang and H. C. Zeng, *ACS Appl. Mater. Interfaces*, 2019, **11**, 23180–23191.

63 D. Jia, H. Gao, L. Xing, X. Chen, W. Dong, X. Huang and G. Wang, *Inorg. Chem.*, 2019, **58**, 6758–6764.

64 P. Li, R. Chen, S. Tian and Y. Xiong, *ACS Sustainable Chem. Eng.*, 2019, **7**, 9566–9573.

65 Q. Chen, R. Wang, F. Lu, X. Kuang, Y. Tong and X. Lu, *ACS Omega*, 2019, **4**, 3493–3499.

66 M. Yu, G. Moon, E. Bill and H. Tüysüz, *ACS Appl. Energy Mater.*, 2019, **2**, 1199–1209.

67 J. Yu, Q. Cao, Y. Li, X. Long, S. Yang, J. K. Clark, M. Nakabayashi, N. Shibata and J.-J. Delaunay, *ACS Catal.*, 2019, **9**, 1605–1611.

68 S. Sirisomboonchai, S. Li, A. Yoshida, X. Li, C. Samart, A. Abudula and G. Guan, *ACS Sustainable Chem. Eng.*, 2019, **7**, 2327–2334.

69 M. Y. Gao, C. B. Sun, H. Lei, J. R. Zeng and Q. B. Zhang, *Nanoscale*, 2018, **10**, 17546–17551.

70 G.-Q. Han, Y.-R. Liu, W.-H. Hu, B. Dong, X. Li, X. Shang, Y.-M. Chai, Y.-Q. Liu and C.-G. Liu, *Appl. Surf. Sci.*, 2015, **359**, 172–176.